Highpressure metamorphic mineralogy of the Martian crust with implications for density and seismic profiles

The Meteoritical Society

Meteoritics & Planetary Science 1–15 (2020)
doi: 10.1111/maps.13535

High-pressure metamorphic mineralogy of the Martian crust with implications for density and seismic profiles

Julia SEMPRICH *[1,2], and Justin FILIBERTO [1]

[1]Lunar and Planetary Institute, USRA, 3600 Bay Area Blvd., Houston, Texas77058,USA
[2]AstrobiologyOU, School of Environment, Earth and Ecosystem Sciences, The Open University, Walton Hall, Milton KeynesMK7 6AA,UK
*Corresponding author. E-mail: julia.semprich@open.ac.uk

(Received 29 October 2019; revision accepted 19 May 2020)

Abstract–Here, we calculate the mineralogy of the Martian lower crust and upper mantle as a function of pressure and temperature with depth using four bulk compositions (average crust, Gusev basalt, olivine-phyric shergottite, and primitive average mantle). We then use this mineralogy to extract rock properties such as density and seismic velocities, describe their changes with varying conditions and geotherms, and make predictions for the crust–mantle boundary. Mineralogically, all compositions produce garnet, orthopyroxene, clinopyroxene in varying proportions at high pressures, with differences in minor minerals (spinel, ilmenite, rutile, and/or K-feldspar). According to our calculations, the average crust and Gusev basalt compositions have the potential to yield higher densities than the average mantle composition, particularly for thicker crusts and/or colder geotherms. Therefore, recycling of the Martian crust into the mantle could occur through the process of crustal delamination, if not kinetically inhibited. However, our results show that, depending on crustal thickness, the crust may not be easily distinguishable from the mantle in seismic properties.

INTRODUCTION

Investigating the alteration history of the Martian crust has been a major research and exploration focus because alteration minerals can record the history of past fluids that could have been a habitable environment. However, most of the focus has been on low temperature fluids and the minerals produced at near surface conditions. Understanding the alteration history and mineralogy of the lower crust and upper mantle is critical to unravel the internal structure of Mars and processes at the crust–mantle boundary. Therefore, here we calculate the mineralogy of the lower crust and upper mantle as a function of increased pressure and temperature with depth and use that mineralogy to constrain variations in density and seismic properties.

Secondary mineralogy records the P–T–X_{fluid} conditions of alteration. Alteration minerals have been found in the Martian meteorites, at every landing site, and in the crust from orbit (see reviews in Filiberto and Schwenzer 2019). Extensive thermochemical calculations have been conducted to investigate the range of conditions of alteration providing evidence for mostly lower temperature fluids (<200 °C) and from near-neutral to acidic fluids (e.g., Griffith and Shock 1997; McAdam et al. 2008; Schwenzer and Kring 2013; Zolotov and Mironenko 2016).

Recent work has expanded investigations of alteration minerals to low-grade metamorphic conditions. Evidence for hydrothermal and low-grade metamorphism comes from both spectral investigations of the Martian crust and detailed analyses of Martian meteorites. Filiberto et al. (2014) found evidence for high temperature fluids in the form of marialite (Na-Cl scapolite) in a melt inclusion in Nakhla, which is consistent with formation from Cl-rich, water-poor fluid (either magma or brine) at a minimum temperature of 700 °C. Further evidence for Cl-rich hydrothermal conditions has been found in other nakhlites in the form of Cl-potassic-hastingsite (e.g., Giesting and Filiberto 2016), which forms in medium-grade metamorphic conditions (>400 °C). Finally, recent

investigations of meteorite NW 7533 found eskolaite encased in chromite-magnetite and suggested that it formed from an active hydrothermal environment in the Martian crust (Liu et al. 2016). From orbit, smectite, chlorite, prehnite, phyllosilicates, the zeolite analcime, opaline silica, and serpentine have been detected (e.g., Ehlmann and Edwards 2014). Some of the mineral assemblages require elevated temperatures of formation (McSween et al. 2015). McSween et al. (2015) and Semprich et al. (2019) used metamorphic phase diagrams and phase equilibria models to constrain formation conditions of the minerals detected from orbit. Their results replicate the low-grade metamorphic mineral phases that have been detected on the Martian surface, which could have either formed by impact or magmatic hydrothermal activity or along a somewhat higher geothermal gradient than for present-day Mars.

Better constraints on the composition and processes in the Martian lower crust are crucial to understand the internal structure and for the determination of crustal thickness and evolution by geodynamic models. However, only one paper has experimentally investigated higher metamorphic grade at one single *P–T–X* condition. Papike et al. (2013) experimentally produced an eclogite from a QUE 94201 bulk composition at 4 GPa and 1200 °C. The mineralogy was 54% omphacite, 35% garnet, 6% ilmenite, 4% SiO_2-phase, and trace rutile and phosphate (Papike et al. 2013). While this study shows that an eclogitic assemblage can be produced from Martian compositions, the experimental *P–T* conditions exceed those estimated at the crust–mantle boundary (~0.5 to 2 GPa at 800–1000 °C; Babeyko and Zharkov 2000), even when assuming a crustal thickness exceeding 100 km. Only one study calculated the mineralogy, density, and seismic properties of Martian meteorite basalts up to depths corresponding to the crust–mantle boundary assuming that the shergottites represent the average crust (Babeyko and Zharkov 2000). Their results produce a very dense, overly thick crust for most geotherms; however, recent work has shown that the shergottites do not represent average crust (e.g., Filiberto 2017) and the results from these calculations likely do not represent mineralogy or physical properties of the Martian crust. Specifically, Martian meteorites have higher MgO and FeO and lower Na_2O and K_2O contents than the average crust (e.g., Filiberto 2017), which would produce an overly dense crust if assumed to represent the entire crust. Furthermore, Babeyko and Zharkov (2000) determine the crustal thickness from the condition that densities at the crust–mantle boundary range between 3450 and 3500 kg m^{-3}. However, neither the crust nor the mantle (Bertka and Fei 1998) is expected to reach densities of 3500 kg m^{-3} at pressures ≤1 GPa corresponding to crustal thickness estimates ~100 km (e.g., Wieczorek and Zuber 2004; Baratoux et al. 2014).

Therefore, there are only few constraints on high-grade metamorphism of lower crust/upper mantle, which are important for our understanding of the Martian interior such as crustal thickness and processes at the crust–mantle boundary. Furthermore, better constraints on the properties of the Martian lower crust and upper mantle as a function of compositions and *P–T* conditions will be vital for understanding and interpreting the seismic data returned from the recently landed InSight mission (Smrekar et al. 2018). Here, we expect changes in texture and mineralogy and therefore metamorphic reactions within the Martian crust due to an increase in pressure and temperature with depth by burial without invoking any plate tectonic processes such as subduction or orogeny. Since the mineral assemblages are calculated by Gibbs free energy minimization at any given pressure and temperature and therefore without assuming any metamorphic history, our results are also relevant for igneous rocks that have intruded at depth resulting in high-pressure mineral assemblages (e.g., Medaris et al. 2006, 2018; Müntener and Ulmer 2006). We use the Perple_X software suite (Connolly 2005) to calculate the metamorphic mineralogy of the Martian lower crust and upper mantle for four bulk compositions. We then adopt this mineralogy to extract rock properties such as density and seismic velocities (v_s and v_p), describe their changes with *P–T–X*, and discuss implications for the crust–mantle boundary and how our results can be useful for geodynamic and geophysical models and the interpretation of seismic data.

METHODS AND INPUT PARAMETERS

Bulk Compositions

To investigate a range of bulk compositions (Table 1), we chose the average Martian crust (Taylor and McLennan 2009), the surface basalt analyzed at Gusev Crater: Humphrey (McSween et al. 2006), Martian meteorite Yamato 980459 a primitive, mantle-derived, olivine-phyric shergottite (an average of data calculated by mineral mode and electron microprobe analyses by Greshake et al. [2004]; and wet chemical analyses from Misawa [2004]), and a calculated mantle composition (Taylor 2013). From here on, these will be referred to as: average crust, Gusev basalt, shergottite, and average mantle, respectively (Table 1). These provide a large range of Mg# to explore. We assume water-free conditions in our calculations (1) to be comparable with experimental work on high-pressure

Table 1. Bulk compositions used for phase equilibria and rock property calculations.

wt%	Average crust*	Gusev basalt† Humphrey	Shergottite‡ meteorite: Yamato 980459	Average mantle§ Primitive silicate mantle
SiO_2	49.3	45.9	49.33	43.7
TiO_2	0.98	0.58	0.52	n.u.
Al_2O_3	10.5	10.68	5.48	3.04
Cr_2O_3	n.u.	n.u.	0.7	0.7
FeO	18.2	18.6	17.17	18.1
MgO	9.06	10.41	18.81	30.5
CaO	6.92	7.84	6.57	2.43
Na_2O	2.97	2.5	0.65	0.53
K_2O	0.45	n.u.	n.u.	n.u.

n.u. = not used in this study.
*Taylor and McLennan (2009).
†McSween et al. (2006).
‡Greshake et al. (2004); Misawa (2004)
§Taylor (2013).

phase relations (Papike et al. 2013); (2) based on studies of the terrestrial crust, pore water is typically squeezed out of the system by compaction and diagenesis (e.g., Heier 1965); and (3) eclogite facies do not typically contain hydrous phases and are relatively anhydrous with between 3000 and 300 ppm H_2O (e.g., Katayama et al. 2006). We assume all iron as Fe^{2+}. The oxygen fugacity of the Martian mantle, as exemplified by the shergottites, is around QFM −3 to +3 (Herd 2003; Righter et al. 2008), which would equate to <5% Fe^{3+}. For Humphrey, similar values in the range of −2.3 to −3.6 have been obtained (Schmidt et al. 2013).

Phase Equilibria Modeling

We followed the same approach from Semprich et al. (2019) for using the Gibbs free energy minimization software Perple_X 6.8.6 (Connolly 2005) and an internally consistent thermodynamic dataset (Holland and Powell 1998, 2011) to calculate metamorphic phase diagrams. We computed phase equilibria for four starting compositions (see next section) in the range 0.1–3 GPa (equivalent to ~10 to 255 km depth) and 500–1100 °C. Mn and P were not considered due to their relatively low abundances and/or incomplete set of solid solution models. Cr was considered in the shergottite and average mantle compositions, while K has only been added to the average Martian crust but is negligible for all other compositions. Furthermore, Ti was not considered for the average mantle composition due to its low abundance. For the average crust and Gusev basalt compositions, we used the following solid solution models: olivine (Holland and Powell 1998), omphacite (Green et al. 2007), garnet and orthopyroxene (White et al. 2014), feldspar (Fuhrman and Lindsley 1988) for calculations with K, plagioclase (Newton et al. 1980) for calculations without K, spinel (White et al. 2002), and ilmenite (White et al. 2000). A similar set of solid solution models was used for the shergottite except for clinopyroxene (Holland and Powell 1996), garnet, and spinel (Jennings and Holland 2015). For the average mantle composition, the following solid solutions were used: olivine, orthopyroxene, garnet, spinel (Jennings and Holland 2015), clinopyroxene (Holland and Powell 1996), and plagioclase (Newton et al. 1980).

Densities as well as seismic velocities were extracted from the phase diagrams using the Perple_X application werami according to the approach described by Connolly and Kerrick (2002). Herewith, the compressional- (v_P) and shear-wave (v_S) velocities are described as a function of three thermodynamic properties: the density (ρ), the adiabatic bulk modulus (K_S), and the shear modulus (μ) in the following equations for an isotropic, homogeneous material (Bina and Helffrich 1992; Karki et al. 2001):

$$v_P = \sqrt{\frac{K_S + 4\mu/3}{\rho}};\ v_S = \sqrt{\frac{\mu}{\rho}}. \tag{1}$$

Both the density and the adiabatic bulk modulus can be expressed as a function of Gibbs free energy:

$$\rho = N/\frac{\delta G}{\delta P} \text{and } K_S = -\frac{\delta G}{\delta P}\left[\frac{\delta^2 G}{\delta P^2} + \left(\frac{\delta}{\delta P}\frac{\delta G}{\delta T}\right)^2 / \frac{\delta^2 G}{\delta T^2}\right]^{-1}, \tag{2}$$

with N being the molar formula weight and G the molar free energy (Connolly and Kerrick 2002). The shear modulus for all relevant phases is computed as $3K_S(1-2\nu)/(\nu+1)/2$ where the Poisson ratio ν is set to 0.35. Due to the lack of detailed textural information, the adiabatic bulk and shear moduli are estimated as the weighted average of upper and lower bounds on the moduli. The Voigt–Reuss–Hill (VRH) method (e.g., Berryman 2013) is used in our calculations where the lower bound (Z-) on the modulus Z of an aggregate is calculated as the harmonic mean on the corresponding moduli on its constituent phases (p): $Z_- = 1/(\text{sum}[x_i/Z_i, I = 1...p])$ and the upper bound (Z_+) is given by $Z_+ = \text{sum}(x_i \times Z_i,\ i = 1...p)$, where x_i is the volume fraction of phase i. The aggregate modulus is then calculated as $Z = (1 - \chi) \times Z_- + \chi \times Z_+$, where the weighting factor χ is 0.5 (e.g., Connolly and Kerrick 2002).

Physical Parameters of Mars

The upper crustal layer of 8–11 km is expected to show a high grade of porosity and/or alteration, which has recently been inferred by receiver function analysis of seismic data obtained by the seismometer of the InSight lander at Elysium Planitia (Lognonné et al. 2020). Since our study focuses on consolidated rocks, we start our calculations at 10 km (~0.1 GPa) depth below the high porosity layer. Large quakes or located impacts that could provide constraints on the composition of the lower crust and upper mantle and the location of the crust–mantle boundary have not yet been detected on Mars (Lognonné et al. 2020). Therefore, estimates of the mean Martian crustal thickness are based on indirect studies such as local relationships between gravity and topography or geochemical observations and range between 30 and 80 km (Zuber et al. 2000; Neumann et al. 2004; Wieczorek and Zuber 2004; Parro et al. 2017). However, crustal thicknesses of up to 100 km are consistent with global geophysical constraints (Sohl and Spohn 1997; Kavner et al. 2001; Gudkova and Zharkov 2004). An upper limit of 150 km may be possible based on the recalculation of the moment of inertia factor (e.g., Sohl et al. 2005) although viscous relaxation arguments suggest that the average crust does not exceed 100 km (Zuber et al. 2000; Nimmo and Stevenson 2001). While our calculated phase diagrams and extracted densities and seismic velocities cover depths in the range of ~10 and 250 km, we also compared rock and mineral properties for all compositions at specific depths of 50 and 150 km at temperatures of 700 and 1000 °C, relevant for cold and warm geotherms, respectively.

Due to the lack of in situ measurements, estimates of the surface heat flux of Mars are also based on indirect methods depending on several parameters that are currently not well constrained, such as abundance of heat-producing elements, topography, as well as crust and mantle thickness and densities (e.g., McGovern et al. 2002, 2004; Plesa et al. 2016; Parro et al. 2017). The present-day heat flux shows regional differences and is modeled in most regions to vary between 14 and 25 mW m^{-2} (Parro et al. 2017), 11–50 mW m^{-2} (McGovern et al. 2004), and 17.2–49.9 mW m^{-2} (Plesa et al. 2016). These values correspond to a range of geotherms predominantly varying between 3 and 20 K km^{-1} (McGovern et al. 2004). In accordance with these findings, we assume 5, 7, 10, and 20 °C km^{-1} as examples of possible geothermal gradients. Colder geotherms could be relevant for Pavonis Mons and Elysium Rise, while warmer geothermal gradients have been estimated for Noachis Terra and Northeastern Arabia Terra (McGovern et al. 2004).

To estimate depth from pressure, we use the following equation: $h = P/\rho g$, with a gravity (g) value for Mars of 3.727 m s^{-2} and the average crustal density (ρ) of 2900 kg m^{-3}, which is within the range of most Mars models (e.g., McGovern et al. 2004; Sohl et al. 2005; Plesa et al. 2016; Parro et al. 2017). Note that the actual density is not constant and varies as a function of pressure, and hence, the depths given in this work are only a rough approximation (Cammarano 2013).

RESULTS

Mineralogically, all samples are similar with a calculated low pressure assemblage of orthopyroxene, clinopyroxene, and olivine dominating the mineralogy with either plagioclase-rich feldspar (average crust composition due to addition of *K*) or plagioclase and ilmenite (average crust, Gusev basalt, shergottite) or spinel (shergottite and average mantle compositions) as accessory phases. Figure 1 shows the calculated proportions of olivine, clinopyroxene, plagioclase (feldspar), and garnet, as well as the fayalite (Fe_2SiO_4) component in olivine, diopside ($CaMgSi_2O_6$) component in clinopyroxene, anorthite ($CaAl_2Si_2O_8$) component in plagioclase, and almandine ($Fe_3Al_2Si_3O_{12}$) component in garnet in addition to the mineral assemblages for all four compositions. In the average crust and Gusev basalt, the modal amount of olivine ranges between ~29 and 25 vol% (Figs. 1a and 1e).The fayalite component decreases with increasing temperature and is in the range of 0.59–0.63 (Fa_{59-63}) in the average crust (Fig. 1a) and Fa_{54-56} in the Gusev basalt (Fig. 1e). Olivine proportions in the shergottite at low pressures are ~10 vol% with Fa_{40} (Fig. 1i) and ~59 vol% in the average mantle composition with Fa_{25} (Fig. 1m). The average crust and Gusev basalt contain 15–20 vol% clinopyroxene with Di_{50-65} (lower values at higher temperature) in the average crust (Fig. 1b) and Di_{60-70} in the Gusev basalt (Fig. 1f). The shergottite contains ~22 to 25 vol% clinopyroxene with Di_{62-77} (Fig. 1j), while the average mantle contains ~4 to 7 vol% clinopyroxene with Di_{70-80} (Fig. 1n). Plagioclase in the average crust and Gusev basalt is present up to ~50 vol% with An_{30-34} and 9–12 vol% in the shergottite and average mantle with An_{40-50}.

As the pressure increases in our modeled phase diagrams, the modal amounts of olivine and plagioclase in the average crust and Gusev basalt start to decrease and are being replaced by garnet and omphacitic clinopyroxene (Figs. 1a, 1b, 1d, 1e, 1f, 1h). These reactions are shifted toward higher pressure with increasing temperature. In the Gusev basalt, shergottite, and average mantle, olivine is stable within all

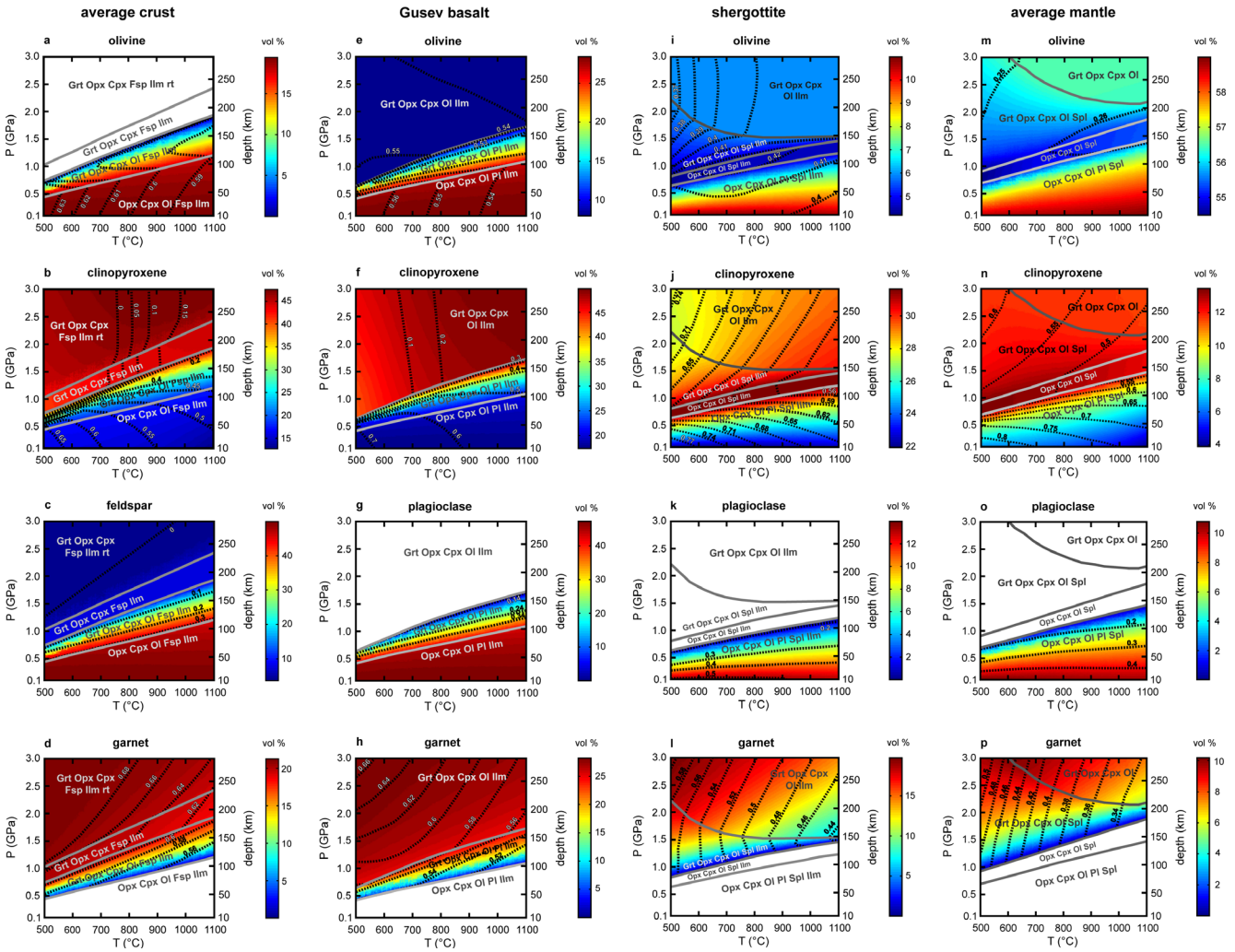

Fig. 1. Modal proportions of olivine, clinopyroxene, feldspar/plagioclase, and garnet in vol% for the average crust, Gusev basalt, shergottite, and average mantle compositions (Table 1) overlain by mineral phase diagram. Dashed lines and numbers represent the forsterite (Fo) component in olivine, the diopside (Di) component in clinopyroxene, the anorthite (An) component in feldspar/plagioclase, and the almandine (Alm) component in garnet. Mineral abbreviations: Cpx—clinopyroxene; Fsp—feldspar; Grt—garnet; Ilm—ilmenite; Ol—olivine, Opx—orthopyroxene; Pl—plagioclase; rt—rutile; Spl—spinel.

calculated pressure and temperature conditions but decreases with increasing pressure before slightly increasing again in the shergottite and average mantle toward the highest pressure considered (Figs. 1i and 1m). At higher pressures, the remaining plagioclase reacts out for Gusev basalt (Fig. 1g), while the remaining feldspar in the average crust is rich in sanidine component due to the K-bearing composition (Fig. 1c). Plagioclase in the shergottite and average mantle is first replaced by spinel and then by garnet as pressure increases (Figs. 1k, 1o, 1l, and 1p). The high-pressure assemblage for all compositions contains garnet, orthopyroxene, and clinopyroxene in varying proportions. The average crust and Gusev basalt contain ~45 to 50 vol% clinopyroxene with $Di_{0\text{-}20}$, 20–28 vol% garnet with $Alm_{56\text{-}68}$, and 14–27 vol% orthopyroxene at the highest pressure of 3 GPa. The shergottite shows 27–30 vol% clinopyroxene ($Di_{56\text{-}74}$), 15–20 vol% garnet ($Alm_{46\text{-}58}$), and 45–49 vol% orthopyroxene, while the average mantle has ~11 vol% clinopyroxene ($Di_{50\text{-}60}$), 8–10 vol% garnet ($Alm_{34\text{-}50}$), and 21–24 vol% orthopyroxene. Olivine is stable in the Gusev basalt (~8 to 10 vol%), shergottite (~5 to 6 vol%), and average mantle (~56 vol%) at high pressures. The average crust composition contains feldspar (<4 vol%), ilmenite (<0.3 vol%), and rutile (<0.8 vol%) as accessory phases due to K and Ti being considered in the starting composition; the shergottite contains ilmenite and the average mantle composition shows spinel at the lowest temperatures in the phase

diagram. This mineralogy is similar to the experimental work on a QUE 94201 bulk composition at 4 GPa and 1200 °C, which produced 54% omphacite, 35% garnet, 6% ilmenite, 4% SiO_2-phase, and trace rutile and phosphate (Papike et al. 2013). This mineralogy is also comparable to the results of Babeyko and Zharkov (2000) for basaltic shergottites with orthopyroxene, clinopyroxene, and garnet dominating the higher pressure assemblages and only minor amounts of quartz. Due to composition and model conditions, our calculated phase diagrams do not contain quartz at higher pressures.

Modeled densities range from 3100 to 3650 kg m^{-3} for all bulk compositions, but there are important differences of how density varies with pressure and temperature for each bulk composition (Fig. 2). In Table 2, we have extracted mineral and system properties including modal mineral proportions, densities, and seismic velocities for all compositions at specific conditions of 0.5 GPa and 700 °C; 0.5 GPa and 1000 °C; 1.55 GPa and 700 °C; 1.55 GPa and 1000 °C. The lower pressures approximately represent a 50 km thick crust assuming different temperature profiles, while the latter two conditions represent an overly thick crust of approximately 150 km (these depths are shown by the dashed red lines in Fig. 2).

The average crust and Gusev basalt compositions show the lowest densities at low pressures (Figs. 2a and 2b). This is due to the high modal amount of low-density feldspar/plagioclase (~2600 to 2650 kg m^{-3}, Table 2). At pressure conditions of 0.5 GPa (~50 km) and temperatures of 700 and 1000 °C, respectively, the assemblage consists of 45–49 vol% feldspar/plagioclase resulting in rock densities in the range of 3100–3174 kg m^{-3} with variations in density mainly caused by changes in mineral composition (with Fe-bearing endmembers showing higher densities than Mg-bearing ones) and to a lesser extent by expansion and compression due to higher temperatures and pressures (Table 2). With increasing pressure, plagioclase and olivine react to form orthopyroxene, clinopyroxene, and garnet (Figs. 1a–h). This transition starts at higher pressures in the average crust compared to the Gusev basalt and causes significant densification in both compositions (Figs. 2a and 2b). At 1.55 GPa (~150 km) and both temperatures considered, the modal amount of garnet is 16–27 vol% with densities in the range of 3914–4029 kg m^{-3} (Table 2). At conditions where feldspar/plagioclase is either absent or only present in low proportions, rock densities of the compositions exceed 3500 kg m^{-3} (Table 2). Only the crustal composition at 1.55 GPa and 1000 °C contains a significant amount of feldspar/plagioclase (~23 vol%) and hence yields a lower density of 3357 kg m^{-3}. Figure 2 also demonstrates that a hot geotherm of 20 °C km^{-1} is located within the feldspar/plagioclase-rich mineral assemblage for the average crust and Gusev basalt composition and hence will never exceed a density of ~3200 kg m^{-3}. The 10 °C km^{-1} geotherm, however, is partly (crustal composition) and completely (Gusev basalt) within the garnet stability field, but not yet in the area of significant densification. Even colder geotherms of 7 and 5 °C km^{-1} are well into the garnet stability field and both compositions could show significant densification in regions where the crustal thickness exceeds 100 km. In areas of lower crustal thickness, the cold geotherms will not be hot enough (>700 °C) for the rock compositions to equilibrate, and therefore, they will likely be preserved as a metagabbro with lower densities.

The shergottite and average mantle compositions are significantly denser (3320–3370 km m^{-3}) at low pressures than the average crust and Gusev basalt (Figs. 2c and 2d; Table 2). However, due to their low Al_2O_3 content in the whole rock composition, the amount of Al-bearing phases (plagioclase, spinel, and garnet) is significantly lower resulting in less significant densification with pressure (~3418 to 3493 kg m^{-3} at 1.55 GPa and both temperatures). Geotherms of 20 and 10 °C km^{-1} are completely within the spinel stability field, while only the coldest geotherm of 5 °C km^{-1} is within the garnet stability field.

Seismic properties (v_P and v_S) follow the same pattern as mineralogy and density (v_P in Fig. 3 and v_S in Fig. S1 in supporting information; Table 2). All compositions have similar ranges in v_P and v_S but show significant differences in how seismic velocities change with pressure. The average crust and Gusev basalt compositions show a more significant increase in seismic velocities with increasing pressure from v_P ~ 6.07–6.31 km s^{-1} (v_S ~ 2.92–3.03 km s^{-1}) at 0.5 GPa to v_P ~ 6.68–7.31 km s^{-1} (v_S ~ 3.21–3.41 km s^{-1}) due to the formation of garnet, clinopyroxene, and orthopyroxene at the expense of plagioclase and olivine. The shergottite and average mantle compositions, however, show more gradual increases in both v_P (6.38–6.82 km s^{-1} at 0.5 GPa; 6.77–7.12 km s^{-1} at 1.55 GPa) and v_S (3.06–3.28 km s^{-1} at 0.5 GPa; 3.25–3.42 km s^{-1} at 1.55 GPa) with increasing pressure.

Subtracting densities of the average mantle composition from those of the average crust and Gusev basalt, respectively (Fig. 4), shows at which conditions the density of the average crust and the Gusev basalt exceed that of the average mantle. Both compositions are denser than the average mantle at pressures exceeding 1 GPa (~100 km) at 600 °C, but the density crossover is shifted toward higher pressures with increasing temperatures. If the crust can get denser than

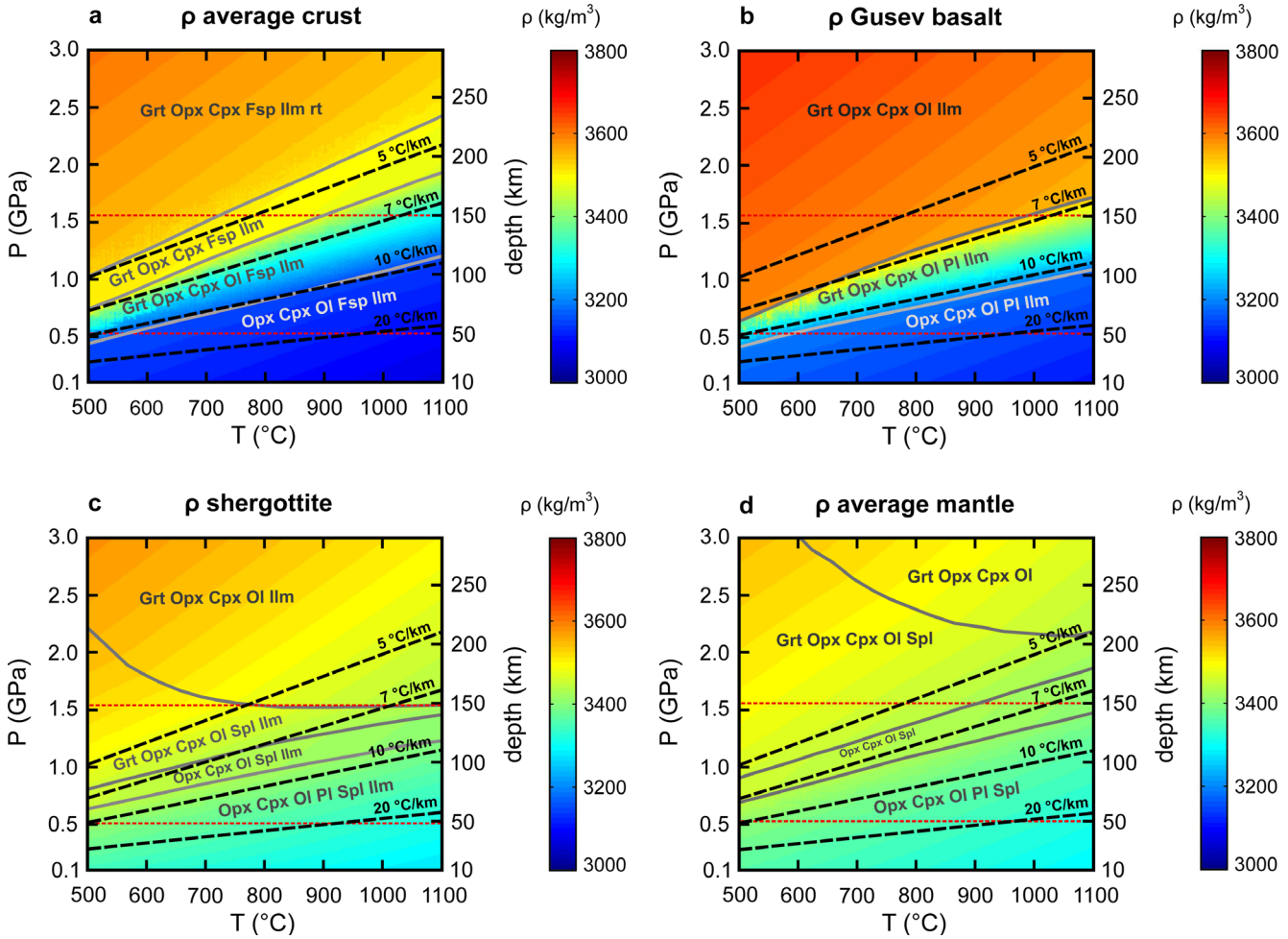

Fig. 2. Calculated densities (kg m^{-3}) overlain by mineral phase diagram for (a) average crust, (b) Gusev basalt, (c) shergottite, and (d) average mantle (bulk compositions in Table 1). Dashed black lines represent approximate geotherms varying from 5 to 20 °C km^{-1}. Dashed red horizontal lines represent crustal depths of 50 and 150 km, at which mineral and rock properties are extracted (Table 2). The depth scale shown is approximated by the formula: $h = P/\rho g$, with a gravity (g) value for Mars of 3.727 m s^{-2} and an average crustal density (ρ) of 2900 kg m^{-3}.

the mantle depends on several factors including the crustal composition, crustal thickness, and the exact geotherm; thicker crusts and colder geotherms are more favorable for a density crossover.

DISCUSSION

Implications for Crustal Properties and the Crust–Mantle Boundary

The range of our calculated densities (3100–3650 kg m^{-3}) for the lower crust overlaps with that obtained by Baratoux et al. (2014) derived from major element chemistry of Martian meteorites, in situ measurements by rovers, and from surface geochemistry with values in the range of 3100–3700 kg m^{-3}. However, our diagrams show that densities above 3300 kg m^{-3} for both the crustal and the basaltic compositions are only attained above ~0.7 GPa corresponding to depths of ~60 km. Density changes as a function of mineralogy and therefore with pressure and temperature. While lower temperatures are generally more favorable for higher densities since the transition to eclogite is shifted toward lower pressures, slow reaction kinetics will prevent mineral reactions below a certain temperature. Babeyko and Zharkov (2000) assume a "freezing" temperature for dry basalts at ~700 to 800 °C. As a result, the mineralogy of the rock will not change despite a decrease in surrounding temperatures. Calculating densities for Martian basalts at 1 bar and 25 °C, as Baratoux et al. (2014) have done in their study, will therefore yield higher densities than the actual values. For example, measured grain densities (porosity free) of the Zagami basaltic shergottite range

Table 2. Mineral and rock properties for all rock compositions at selected pressure and temperature conditions.

	Average crust				Gusev basalt				Shergottite				Average mantle			
	vol.%	ρ (kg m^{-3})	v_P (km s^{-1})	v_S (km s^{-1})	Vol.%	ρ (kg m^{-3})	v_P (km s^{-1})	v_S (km s^{-1})	vol.%	ρ (kg m^{-3})	v_P (km s^{-1})	v_S (km s^{-1})	Vol.%	ρ (kg m^{-3})	v_P (km s^{-1})	v_S (km s^{-1})
0.5 GPa (~50 km), 700 °C																
Fsp/Pl	48.76	2625	5.74	2.76	45.78	2648	5.85	2.81	7.81	2623	5.69	2.73	7.97	2627	5.74	2.74
Opx	14.56	3525	6.29	3.02	7.1	3513	6.28	3.01	55.99	3436	6.34	3.05	25.39	3358	6.42	3.09
Cpx	16.43	3324	7.04	3.38	18.53	3310	7.05	3.39	26.29	3293	7.06	3.39	7.97	3273	7.08	3.4
Ol	18.98	3883	6.72	3.23	27.82	3822	6.78	3.26	8.11	3654	6.96	3.34	57.75	3472	7.16	3.44
Ilm	1.26	4594	6.98	3.35	0.77	4580	6.99	3.36	0.71	4533	7.03	3.38	–	–	–	–
Spl	–	–	–	–	–	–	–	–	1.09	4306	7.92	3.81	0.92	4307	7.92	3.81
System	100	3135	6.17	2.97	100	3174	6.31	3.03	100	3370	6.52	3.13	100	3367	6.82	3.28
0.5 GPa (~50 km), 1000 °C																
Fsp/Pl	48.84	2604	5.64	2.71	46.17	2628	5.75	2.76	9.24	2611	5.64	2.71	8.55	2611	5.64	2.71
Opx	15.75	3473	6.2	2.98	6.78	3468	6.12	2.94	54.57	3390	6.18	2.97	26.07	3319	6.26	3.01
Cpx	15.11	3320	6.91	3.32	18.24	3306	6.92	3.33	25.3	3280	6.93	3.33	6.46	3251	6.95	3.34
Ol	19.05	3812	6.67	3.20	28.05	3760	6.72	3.23	8.83	3603	6.89	3.31	58.26	3431	7.08	3.40
Ilm	1.26	4502	6.81	3.27	0.77	4484	6.82	3.28	0.71	4419	6.87	3.3	–	–	–	–
Spl	–	–	–	–	–	–	–	–	1.02	4281	7.86	3.78	0.65	4284	7.86	3.77
1.55 GPa (~150 km), 700 °C																
Fsp/Pl	4.58	2580	5.88	2.82	–	–	–	–	–	–	–	–	–	–	–	–
Opx	28.44	3571	6.45	3.1	16.95	3525	6.49	3.12	52.12	3448	6.58	3.16	27.32	3378	6.66	3.2
Cpx	45.55	3360	7.26	3.49	47.38	3344	7.26	3.49	29.05	3319	7.22	3.47	12.64	3312	7.27	3.49
Ol	–	–	–	–	8	3841	6.89	3.31	5.81	3671	7.07	3.39	55.48	3503	7.25	3.48
Grt	20.42	4029	8.12	3.9	26.8	3983	8.14	3.91	12.18	3949	8.15	3.91	3.8	3853	8.21	3.94
Ilm	0.43	4636	7.14	3.43	0.87	4611	7.16	3.44	0.73	4563	7.2	3.46	–	–	–	–
Spl	–	–	–	–	–	–	–	–	0.12	4341	7.98	3.83	0.77	4335	7.99	3.84
rt	0.58	4199	8.73	4.19	–	–	–	–	–	–	–	–	–	–	–	–
System	100	3531	7.11	3.41	100	3597	7.31	3.51	100	3493	6.97	3.35	100	3465	7.12	3.42
1.55 GPa (~150 km), 1000°C																
Fsp/Pl	23.12	2602	5.7	2.74	4.7	2617	5.65	2.71	–	–	–	–	–	–	–	–
Opx	19.47	3521	6.33	3.04	14.44	3499	6.33	3.04	55.54	3418	6.41	3.08	31.27	3356	6.48	3.11
Cpx	32.58	3347	7.12	3.42	45.46	3333	7.15	3.43	30.07	3313	7.1	3.41	12.62	3295	7.16	3.44
Ol	7.21	3853	6.76	3.25	10.06	3794	6.82	3.28	5.91	3639	6.98	3.35	55.28	3467	7.17	3.45
Grt	16.27	3938	8.1	3.89	24.48	3914	8.12	3.9	7.75	3900	8.08	3.88	–	–	–	–
Ilm	1.35	4540	6.99	3.36	0.85	4519	7	3.36	0.73	4457	7.05	3.39	–	–	–	–
Spl	–	–	–	–	–	–	–	–	–	–	–	–	0.83	4292	7.94	3.81
System	100	3357	6.68	3.21	100	3522	7.12	3.41	100	3445	6.77	3.25	100	3418	6.95	3.34

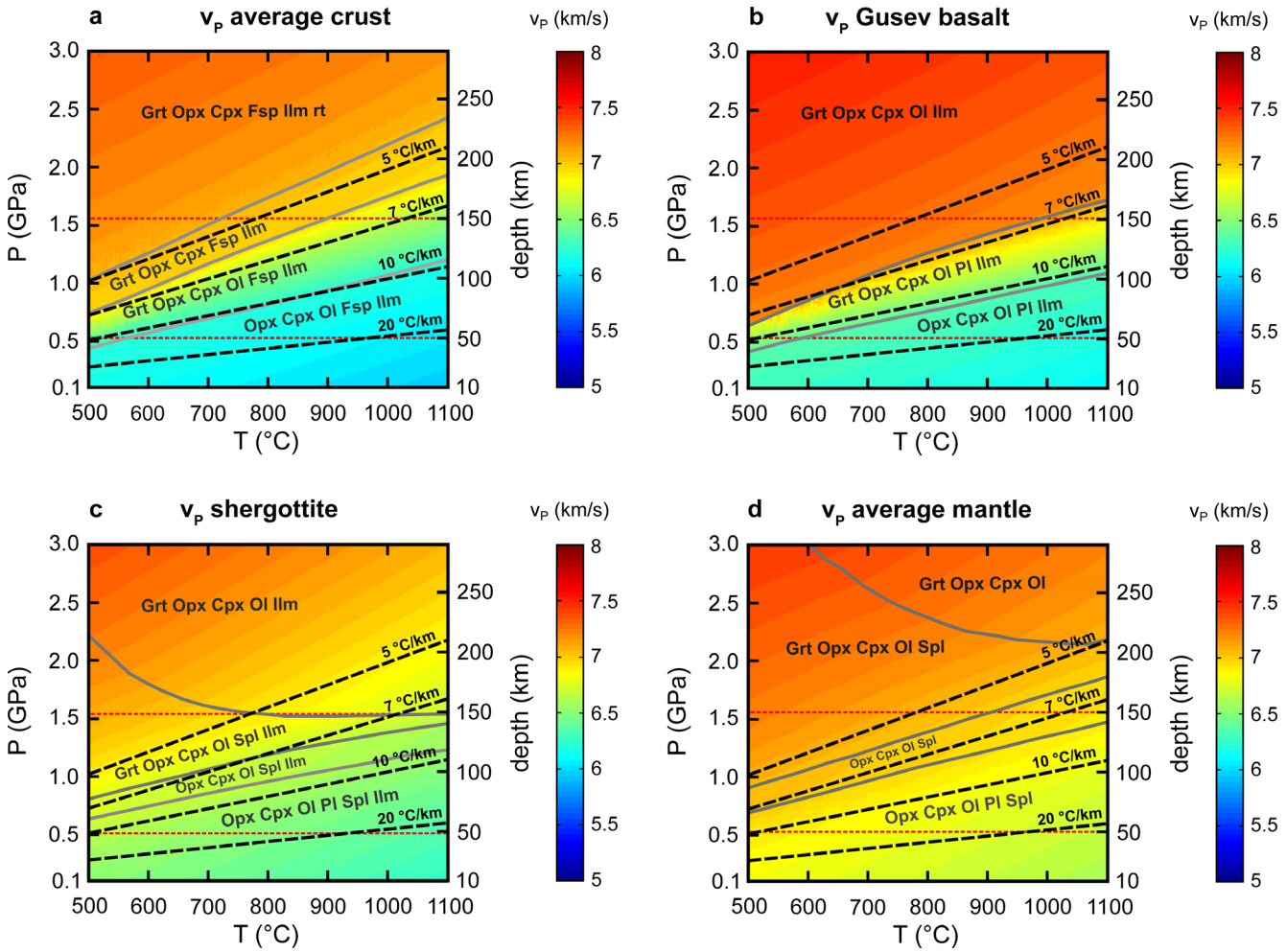

Fig. 3. a–d) Calculated P-wave velocities (km s^{-1}) overlain by mineral phase diagram for compositions as in Fig. 1 (bulk compositions in Table 1).

between 3250 and 3300 kg m^{-3} (Macke et al. 2011), whereas the calculated values of Baratoux et al. (2014) are above 3300 kg m^{-3}.

While our calculations focus on conditions relevant for the lower crust, the low-pressure assemblage of orthopyroxene, clinopyroxene, olivine, feldspar/plagioclase, and ilmenite is stable at pressures relevant to surface conditions. If the crust is ~50 km thick, the density values will thus not exceed 3100 kg m^{-3} and will likely be reduced significantly in the upper few kilometers due to impact cratering and increased porosity. However, in areas where the crust exceeds 50 km, higher densities in the lower section of the lower crustal column are likely. Based on their observations, Baratoux et al. (2014) argue for an average crustal density above 3100 kg m^{-3}, which would be compatible with the mass of Mars and the moment of inertia factor if the average crustal thickness approaches 100 km. In contrast, the majority of geophysical models assume a conservative range of crustal densities within 2700–3100 kg m^{-3} resulting in crustal thickness estimates of 50 ± 12 km (e.g., Wieczorek and Zuber 2004; Sohl et al. 2005). The thickness of the crust significantly influences rock properties at the crust–mantle boundary. Our results suggest a density contrast at the crust–mantle boundary of ≥200 kg m^{-3} at a crustal thickness of ~50 km but <100 kg m^{-3} at a crustal thickness of ~100 km (Fig. 4) with the possibility of a density crossover for basaltic compositions at colder temperatures.

Relevance to Mars

Martian models of crustal thickness and heat flux are dependent on numerous parameters, which are not well constrained and therefore vary considerably. Modeled crustal thicknesses vary predominantly between 30 and 80 km depending on regional

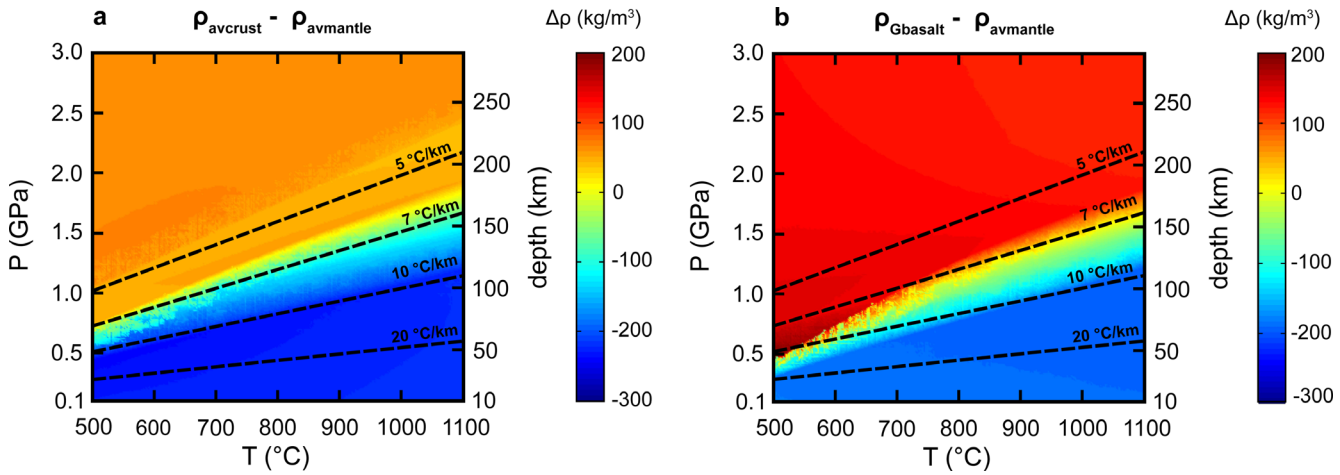

Fig. 4. Density difference between crust and mantle using the computed densities in Fig. 2. a) The density of the average mantle subtracted from the density of average crust; (b) the density of the average mantle subtracted from the density of the Gusev basalt composition. Negative numbers represent conditions where the mantle is denser than the crustal compositions. Positive numbers imply that the density of the crustal composition exceeds that of the mantle.

differences but can reach 100 km with an upper limit of 150 km (e.g., Zuber et al. 2000; Gudkova and Zharkov 2004; Neumann et al. 2004; Sohl et al. 2005; Parro et al. 2017). The present-day heat flux also shows considerable regional differences and is modeled to be in the range of 11–50 mW m^{-2} (e.g., McGovern et al. 2004; Plesa et al. 2016; Parro et al. 2017). Given this wide range of values, we have picked four regions as examples demonstrating how different crustal depths and geotherms can influence crustal densities: Capri Chasma in Valles Marineris, Noachis Terra, as well as Pavonis Mons and Arsia Mons in the Tharsis region. It is also important to note that the heat flux presently modeled in these areas may have changed over geological time and the crust may show different features than described below.

Capri Chasma is located in Valles Marineris, a large canyon system with an estimated crustal depth of 40 km (Neumann et al. 2004) and a thermal gradient of <7 °C km^{-1} (McGovern et al. 2004). The combination of a relatively shallow crust and a cold geotherm does not result in temperatures high enough to cause significant mineralogical changes in the average crust or Gusev basalt compositions until the crust–mantle boundary and there is no significant densification. Due to likely changes in textures with increasing overload pressure, we have labeled these rocks metagabbro (Fig. 5). The average mantle composition at 40 km is in the plagioclase and spinel stability field due to the cold geothermal gradient and will likely not equilibrate until high enough temperatures are reached at much greater depth.

Noachis Terra is an extensive southern landmass west of the Hellas impact basin. The average crustal depth is in the range of 60 km (Neumann et al. 2004) with a geothermal gradient of >20 °C km^{-1} (McGovern et al. 2004). Due to the hot geotherm, the rock compositions will always stay within the plagioclase stability field and no significant densification is expected (Fig. 5). The average mantle composition at the crust–mantle boundary is also expected to be within the plagioclase and spinel stability field.

Pavonis Mons and Arsia Mons are both shield volcanoes in the Tharsis region with crustal depth estimates in the range of 80–100 km (Neumann et al. 2004) and geothermal gradients of >5 °C km^{-1} for Pavonis and <10 °C km^{-1} for Arsia (McGovern et al. 2004). The combination of a thick crust and cold geotherm in the case of Pavonis Mons results in temperatures too low to equilibrate the rocks to higher grade mineralogy and therefore a lack of significant densification. A warmer geotherm as estimated for Arsia Mons combined with a crustal depth of up to 100 km, however, allows for pressures and temperatures high enough to change the mineralogy to garnet-bearing granulite. Igneous rocks intruding at these depths will also show this mineralogy. If the crustal depth exceeds 100 km at geotherms between 10 and 7 °C km^{-1}, at least the Gusev basalt has the potential to become denser than the mantle.

Density Overturn and Delamination

Although the average crust and Gusev basalt compositions show a similar mineralogy, the Gusev basalt is enriched in MgO and CaO compared to the average crust, which results in higher modal proportions

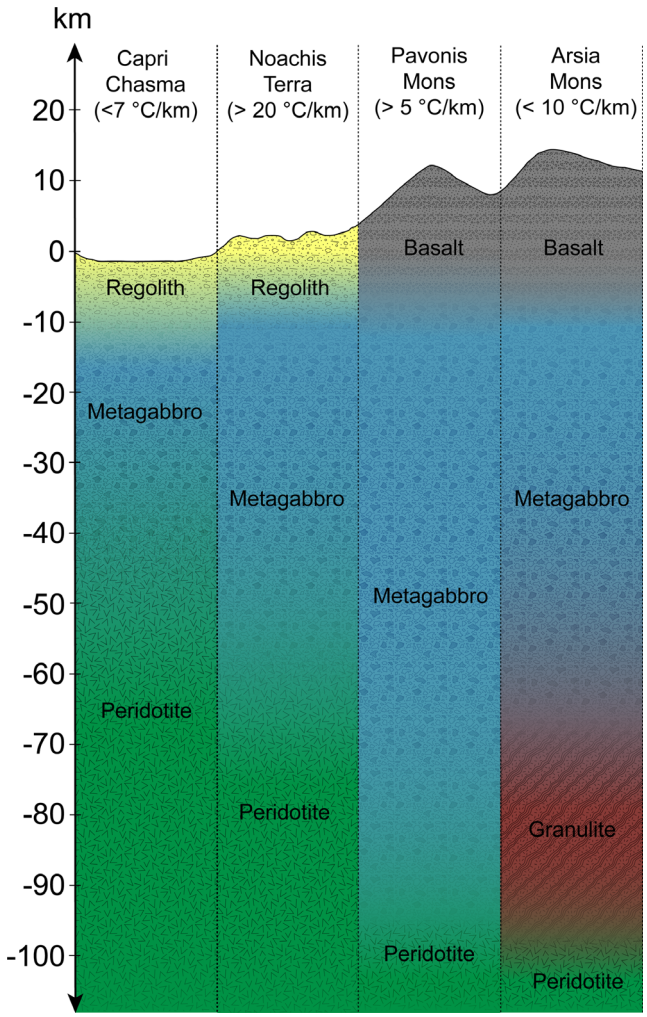

Fig. 5. Crust and upper mantle sections for four different regions on Mars representing several modeled geothermal gradients and crustal thickness. Crustal thickness varies from ~40 km for Capri Chasm, to ~100 km for Pavonis Mons and Arsia Mons.

of garnet. Consequently, the Gusev basalt yields higher densities and seismic velocities even before the transition to eclogite is complete. Hence, small compositional differences can have a significant influence on rock properties and may be of importance for phase transitions and the location of the crust–mantle boundary.

According to our calculations, the crustal compositions considered have the potential to yield higher densities than the average mantle at a crustal thickness exceeding 100 km and for colder geotherms. Therefore, recycling of the Martian crust into the mantle could occur through the process of crustal delamination. However, delamination only takes place if the thermal and compositional parameters are favorable for rheological decoupling (e.g., Ueda et al. 2012). Such a process of gravitational lithospheric instability (or delamination) causing recycling has been proposed for continental regimes in the Earth, Venus, and early Mars (Breuer and Spohn 2003; Elkins-Tanton et al. 2007; Johnson et al. 2014) and may help explain the high potassium of rocks at Gale Crater through mantle metasomatism (Filiberto 2017).

However, a thicker crust not only exposes the root to higher pressures but also increased temperatures. Higher temperatures are less favorable for densification and may therefore prevent delamination (Semprich and Simon 2014), in particular when temperatures above 1000 °C are required to ensure low viscosity of the underlying mantle (Kukkonen et al. 2008). Lower temperatures may not be favorable for mineral reactions and the lower crust may therefore be preserved in a metastable state or only partially reacted to eclogite in the absence of water. Fluids play an important role in the Earth's crust (Putnis and John 2010) and their absence may inhibit eclogitization and densification (e.g., Leech 2001). However, it is not clear how much fluid is required to trigger mineral reactions. Experiments have shown that very low water concentrations in the range of ppm are sufficient for diffusion and mineral growth (e.g., Milke et al. 2009). Water contents in apatite suggest that the Martian mantle source region to the shergottites, chassignites, and nakhlites contains 36–290 ppm H_2O and that the bulk Martian crust has ~1410 ppm H_2O (Filiberto et al. 2016; McCubbin et al. 2016). These values may be enough for mineral reactions but not to form water-bearing minerals such as amphiboles.

Relevance to Geodynamic Models and the Interpretation of Seismic Data

Due to the lack of seismic constraints, neither the crust–mantle boundary nor the densities of the lower crust and upper mantle can be determined without uncertainties. We consider only a few options as lower crustal compositions, which are based on meteorite compositions and in situ measurements of surface rocks. While the lower crust is assumed to be basaltic, the chosen compositions may not adequately reflect Mars' lower crust. Furthermore, variations in crustal composition and properties are expected for a planet of Mars' size.

This study provides pressure–temperature and composition-dependent density and seismic velocity grids that can be implemented into geodynamic and geophysical models to constrain the Martian interior structure and to model processes at the crust–mantle boundary. Furthermore, our seismic velocity diagrams

can help improve radially symmetric Mars models by providing mineralogically realistic seismic velocities of the lower portion of the crust. In addition, the seismic velocities calculated in this study can facilitate the determination of the composition of the lower crust once InSight receives seismic data from the Martian interior. A crust–mantle boundary at ~50 km could be identified by the relatively large differences in seismic velocities between crustal compositions and the mantle in the range of 0.6–0.7 km s^{-1} and 0.5 km s^{-1} (P-wave) for the average crust and Gusev basalt, respectively. In case of a thicker crust exposed to pressure ~1 GPa, this velocity contrast is 0.5 or less for the average crustal composition and only 0.2–0.4 for the Gusev basalt. As a result, the crust may not be easily distinguishable from the mantle and the identification of a crust–mantle boundary may be difficult.

CONCLUSIONS

Our calculations show that compositional differences of possible Martian lower crust can have a significant influence on densities and seismic velocities despite their similar mineral assemblages. At crustal thicknesses of ~50 km, we expect large density and seismic velocity contrasts between the lower crust and the mantle. A thicker crust and therefore higher pressures in combination with relatively cold geotherms will cause a significant densification of the crustal compositions resulting in very little density and velocity contrasts. Therefore, the crust–mantle boundary may be difficult to identify in seismic profiles. The Gusev basalt composition has the potential to become denser than the mantle if the crustal thickness exceeds ~100 km. Delamination may be possible, if the temperatures required for rheological decoupling are not too high.

Acknowledgments—The authors thank B. Joshi for help with calculations. M. Schmidt and an anonymous reviewer are thanked for their constructive comments on an earlier version of this manuscript and K. Righter for editorial handling. LPI Contribution No. 2371. LPI is operated by USRA under a cooperative agreement with the Science Mission Directorate of the National Aeronautics and Space Administration.

Editorial Handling—Kevin Righter

REFERENCES

Babeyko A. Y. and Zharkov V. N. 2000. Martian crust: A modeling approach. *Physics of the Earth and Planetary Interiors* 117:421–435. https://doi.org/10.1016/S0031-9201(99)00111-9.

Baratoux D., Samuel H., Michaut C., Toplis M. J., Monnereau M., Wieczorek M., Garcia R., and Kurita K. 2014. Petrological constraints on the density of the Martian crust. *Journal of Geophysical Research: Planets* 119:1707–1727. https://doi.org/10.1002/2014JE004642.

Berryman J. G. 2013. Mixture theories for rock properties. In *Rock physics & phase relations*, edited by Ahrens T. J. Hoboken, New Jersey: Wiley. pp. 205–228. doi:https://doi.org/10.1029/RF003p0205

Bertka C. M. and Fei Y. 1998. Density profile of an SNC model Martian interior and the moment-of-inertia factor of Mars. *Earth and Planetary Science Letters* 157:79–88. https://doi.org/10.1016/S0012-821X(98)00030-2.

Bina C. R. and Helffrich G. R. 1992. Calculation of elastic properties from thermodynamic equation of state principles. *Annual Review of Earth and Planetary Sciences* 20:527–552. https://doi.org/10.1146/annurev.ea.20.050192.002523.

Breuer D. and Spohn T. 2003. Early plate tectonics versus single-plate tectonics on Mars: Evidence from magnetic field history and crust evolution. *Journal of Geophysical Research: Planets* 108:5072. https://doi.org/10.1029/2002JE001999

Cammarano F. 2013. A short note on the pressure-depth conversion for geophysical interpretation. *Geophysical Research Letters* 40:4834–4838. https://doi.org/10.1002/grl.50887.

Connolly J. A. D. 2005. Computation of phase equilibria by linear programming: A tool for geodynamic modeling and its application to subduction zone decarbonation. *Earth and Planetary Science Letters* 236:524–541. https://doi.org/10.1016/j.epsl.2005.04.033

Connolly J. A. D. and Kerrick D. M. 2002. Metamorphic controls on seismic velocity of subducted oceanic crust at 100-150 km depth. *Earth and Planetary Science Letters* 204:61–74. https://doi.org/10.1016/S0012-821X(02)00957-3.

Ehlmann B. L. and Edwards C. S. 2014. Mineralogy of the Martian surface. *Annual Review of Earth and Planetary Sciences* 42:291–315. https://doi.org/10.1146/annurev-earth-060313-055024.

Elkins-Tanton L. T., Smrekar S. E., Hess P. C., and Parmentier E. M. 2007. Volcanism and volatile recycling on a one-plate planet: Applications to Venus. *Journal of Geophysical Research: Planets* 112:E04S06. https://doi.org/10.1029/2006JE002793

Filiberto J. 2017. Geochemistry of Martian basalts with constraints on magma genesis. *Chemical Geology* 466:1–14. https://doi.org/10.1016/j.chemgeo.2017.06.009

Filiberto J. and Schwenzer S. P. 2019. *Volatiles in the Martian crust*. Amsterdam, the Netherlands: Elsevier. https://doi.org/10.1016/C2015-0-01738-5

Filiberto J., Treiman A. H., Giesting P. A., Goodrich C. A., and Gross J. 2014. High-temperature chlorine-rich fluid in the Martian crust: A precursor to habitability. *Earth and Planetary Science Letters* 401:110–115. https://doi.org/10.1016/j.epsl.2014.06.003.

Filiberto J., Gross J., and McCubbin F. M. 2016. Constraints on the water, chlorine, and fluorine content of the Martian mantle. *Meteoritics & Planetary Science* 51:2023–2035. https://doi.org/10.1111/maps.12624.

Fuhrman M. L. and Lindsley D. H. 1988. Ternary-feldspar modeling and thermometry. *American Mineralogist* 73:201–215.

Giesting P. A. and Filiberto J. 2016. The formation environment of potassic-chloro-hastingsite in the nakhlites

MIL 03346 and pairs and NWA 5790: Insights from terrestrial chloro-amphibole. *Meteoritics & Planetary Science* 51:2127–2153. https://doi.org/10.1111/maps.12675

Green E., Holland T., and Powell R. 2007. An order-disorder model for omphacitic pyroxenes in the system jadeite-diopside-hedenbergite-acmite, with applications to eclogitic rocks. *American Mineralogist* 92:1181–1189. https://doi.org/10.2138/am.2007.2401

Greshake A., Fritz J., and Stöffler D. 2004. Petrology and shock metamorphism of the olivine-phyric shergottite Yamato 980459: Evidence for a two-stage cooling and a single-stage ejection history. *Geochimica et Cosmochimica Acta* 68:2359–2377. https://doi.org/10.1016/j.gca.2003.11.022

Griffith L. L. and Shock E. L. 1997. Hydrothermal hydration of Martian crust: Illustration via geochemical model calculations. *Journal of Geophysical Research: Planets* 102:9135–9143. https://doi.org/10.1029/96JE02939

Gudkova T. V. and Zharkov V. N. 2004. Mars: Interior structure and excitation of free oscillations. *Physics of the Earth and Planetary Interiors* 142:1–22. https://doi.org/10.1016/j.pepi.2003.10.004

Heier K. S. 1965. Metamorphism and the chemical differentiation of the crust. *Geologiska Föreningen i Stockholm Förhandlingar* 87:249–256. https://doi.org/10.1080/11035896509448906

Herd C. D. K. 2003. The oxygen fugacity of olivine-phyric Martian basalts and the components within the mantle and crust of Mars. *Meteoritics & Planetary Science* 38:1793–1805. https://doi.org/10.1111/j.1945-5100.2003.tb00015.x

Holland T. J. B. and Powell R. 1996. Thermodynamics of order-disorder in minerals; II, Symmetric formalism applied to solid solutions. *American Mineralogist* 81:1425–1437. https://doi.org/10.2138/am-1996-11-1215

Holland T. J. B. and Powell R. 1998. An internally consistent thermodynamic data set for phases of petrological interest. *Journal of Metamorphic Geology* 16:309–343.

Holland T. J. B. and Powell R. 2011. An improved and extended internally consistent thermodynamic dataset for phases of petrological interest, involving a new equation of state for solids. *Journal of Metamorphic Geology* 29:333–383. j.1525-1314.2010.00923.x

Jennings E. S. and Holland T. J. B. 2015. A simple thermodynamic model for melting of peridotite in the system NCFMASOCr. *Journal of Petrology* 56:869–892. https://doi.org/10.1093/petrology/egv020

Johnson T. E., Brown M., Kaus B. J. P., and VanTongeren J. A. 2014. Delamination and recycling of Archaean crust caused by gravitational instabilities. *Nature Geoscience* 7:47–52. https://doi.org/10.1038/ngeo2019

Karki B. B., Stixrude L., and Wentzcovitch R. M. 2001. High-pressure elastic properties of major materials of Earth's mantle from first principles. *Reviews of Geophysics* 39:507–534. https://doi.org/10.1029/2000RG000088

Katayama I., Nakashima S., and Yurimoto H. 2006. Water content in natural eclogite and implication for water transport into the deep upper mantle. *Lithos* 86:245–259. https://doi.org/10.1016/j.lithos.2005.06.006

Kavner A., Duffy T. S., and Shen G. 2001. Phase stability and density of FeS at high pressures and temperatures: implications for the interior structure of Mars. *Earth and Planetary Science Letters* 185:25–33. https://doi.org/10.1016/S0012-821X(00)00356-3

Kukkonen I. T., Kuusisto M., Lehtonen M., and Peltonen P. 2008. Delamination of eclogitized lower crust: Control on the crust–mantle boundary in the central Fennoscandian shield. *Tectonophysics* 457:111–127. https://doi.org/10.1016/j.tecto.2008.04.029

Leech M. L. 2001. Arrested orogenic development: eclogitization, delamination, and tectonic collapse. *Earth and Planetary Science Letters* 185:149–159. https://doi.org/10.1016/S0012-821X(00)00374-5

Liu Y., Ma C., Beckett D., Flannery D., and Allwood A. 2016. Metamorphism on Mars: A view from eskolaite-bearing chromite-magnetite in Northwest. Africa NWA 7533. (abstract #1127). 47th Lunar and Planetary Science Conference. CD-ROM.

Lognonné P., Banerdt W. b, Pike W. t, Giardini D., Christensen U., Garcia R. f, Kawamura T., Kedar S., Knapmeyer-Endrun B., Margerin L., Nimmo F., Panning M., Tauzin B., Scholz J-r, Antonangeli D., Barkaoui S., Beucler E., Bissig F., Brinkman N., Calvet M., Ceylan S., Charalambous C., Davis P., van Driel M., Drilleau M., Fayon L., Joshi R., Kenda B., Khan A., Knapmeyer M., Lekic V., McClean J., Mimoun D., Murdoch N., Pan L., Perrin C., Pinot B., Pou L., Menina S., Rodriguez S., Schmelzbach C., Schmerr N., Sollberger D., Spiga A., Stähler S., Stott A., Stutzmann E., Tharimena S., Widmer-Schnidrig R., Andersson F., Ansan V., Beghein C., Böse M., Bozdag E., Clinton J., Daubar I., Delage P., Fuji N., Golombek M., Grott M., Horleston A., Hurst K., Irving J., Jacob A., Knollenberg J., Krasner S., Krause C., Lorenz R., Michaut C., Myhill R., Nissen-Meyer T., ten Pierick J., Plesa A.-C., Quantin-Nataf C., Robertsson J., Rochas L., Schimmel M., Smrekar S., Spohn T., Teanby N., Tromp J., Vallade J., Verdier N., Vrettos C., Weber R., Banfield D., Barrett E., Bierwirth M., Calcutt S., Compaire N., Johnson C. l., Mance D., Euchner F., Kerjean L., Mainsant G., Mocquet A., Rodriguez Manfredi J. A., Pont G., Laudet P., Nebut T., de Raucourt S., Robert O., Russell C. t, Sylvestre-Baron A., Tillier S., Warren T., Wieczorek M., Yana C., and Zweifel P. 2020. Constraints on the shallow elastic and anelastic structure of Mars from InSight seismic data. *Nature Geoscience* 13:213–220. https://doi.org/10.1038/s41561-020-0536-y

Macke R. J., Britt D. T., and Consolmagno G. J. 2011. Density, porosity, and magnetic susceptibility of achondritic meteorites. *Meteoritics & Planetary Science* 46:311–326. https://doi.org/10.1111/j.1945-5100.2010.01155.x

McAdam A. C., Zolotov M. Y., Mironenko M. V., and Sharp T. G. 2008. Formation of silica by low-temperature acid alteration of Martian rocks: Physical-chemical constraints. *Journal of Geophysical Research: Planets* 113:E08003. https://doi.org/10.1029/2007JE003056

McCubbin F. M., Boyce J. W., Srinivasan P., Santos A. R., Elardo S. M., Filiberto J., Steele A., and Shearer C. K. 2016. Heterogeneous distribution of H_2O in the Martian interior: Implications for the abundance of H_2O in depleted and enriched mantle sources. *Meteoritics & Planetary Science* 51:2036–2060. https://doi.org/10.1111/maps.12639

McGovern P. J., Solomon S. C., Smith D. E., Zuber M. T., Simons M., Wieczorek M. A., Phillips R. J., Neumann G. A., Aharonson O., and Head J. W. 2002. Localized gravity/topography admittance and correlation spectra on Mars: Implications for regional and global evolution. *Journal of Geophysical Research: Planets* 107:19–1-19–25. https://doi.org/10.1029/2002JE001854.

McGovern P. J., Solomon S. C., Smith D. E., Zuber M. T., Simons M., Wieczorek M. A., Phillips R. J., Neumann G. A., Aharonson O., and Head J. W. 2004. Correction to "Localized gravity/topography admittance and correlation spectra on Mars: Implications for regional and global evolution." *Journal of Geophysical Research: Planets* 109: E07007.

McSween H. Y., Wyatt M. B., Gellert R., Bell J. F. III, Morris R. V., Herkenhoff K. E., Crumpler L. S., Milam K. A., Stockstill K. R., Tornabene L. L., Arvidson R. E., Bartlett P., Blaney D., Cabrol N. A., Christensen P. R., Clark B. C., Crisp J. A., Des Marais D. J., Economou T., Farmer J. D., Farrand W., Ghosh A., Golombek M., Gorevan S., Greeley R., Hamilton V. E., Johnson J. R., Joliff B. L., Klingelhöfer G., Knudson A. T., McLennan S., Ming D., Moersch J. E., Rieder R., Ruff S. W., Schröder C., and de Souza Jr. P. A., Squyres S. W., Wänke H., Wang A., Yen A., and Zipfel J. 2006. Characterization and petrologic interpretation of olivine-rich basalts at Gusev Crater, Mars. *Journal of Geophysical Research: Planets* 111:E02S10. https://doi.org/10.1029/2005JE002477.

McSween H. Y., Labotka T. C., and Viviano-Beck C. E. 2015. Metamorphism in the Martian crust. *Meteoritics & Planetary Science* 50:590–603. https://doi.org/10.1111/maps.12330

Medaris L. G., Beard B. L., and Jelínek E. 2006. Mantle-derived, UHP garnet pyroxenite and eclogite in the Moldanubian Gföhl Nappe, Bohemian Massif: A geochemical review, new P-T determinations, and tectonic interpretation. *International Geology Review* 48:765–777. https://doi.org/10.2747/0020-6814.48.9.765

Medaris L. G., Brueckner H. K., Cai Y., Griffin W. L., and Janák M. 2018. Eclogites in peridotite massifs in the Western Gneiss Region, Scandinavian Caledonides: Petrogenesis and comparison with those in the Variscan Moldanubian Zone. *Lithos* 322:325–346. https://doi.org/10.1016/j.lithos.2018.10.013.

Milke R., Kolzer K., Koch-Müller M., and Wunder B. 2009. Orthopyroxene rim growth between olivine and quartz at low temperatures (750–950°C) and low water concentration. *Mineralogy and Petrology* 97:223. https://doi.org/10.1007/s00710-009-0093-y

Misawa K. 2004. The Yamato 980459 olivine-phyric shergottite consortium. *Antarctic Meteorite Research* 17:1–12.

Müntener O. and Ulmer P. 2006. Experimentally derived high-pressure cumulates from hydrous arc magmas and consequences for the seismic velocity structure of lower arc crust. *Geophysical Research Letters* 33:L21308. https://doi.org/10.1029/2006GL027629

Neumann G. A., Zuber M. T., Wieczorek M. A., McGovern P. J., Lemoine F. G., and Smith D. E. 2004. Crustal structure of Mars from gravity and topography. *Journal of Geophysical Research: Planets* 109:E08002. https://doi.org/10.1029/2004JE002262

Newton R. C., Charlu T. V., and Kleppa O. J. 1980. Thermochemistry of the high structural state plagioclases. *Geochimica et Cosmochimica Acta* 44:933–941.

Nimmo F. and Stevenson D. J. 2001. Estimates of Martian crustal thickness from viscous relaxation of topography. *Journal of Geophysical Research: Planets* 106:5085–5098. https://doi.org/10.1029/2000JE001331.

Papike J. J., Burger P. V., Shearer C. K., and McCubbin F. M. 2013. Experimental and crystal chemical study of the basalt–eclogite transition in Mars and implications for Martian magmatism. *Geochimica et Cosmochimica Acta* 104:358–376. https://doi.org/10.1016/j.gca.2012.11.007

Parro L. M., Jiménez-Díaz A., Mansilla F., and Ruiz J. 2017. Present-day heat flow model of Mars. *Scientific Reports* 7:45629. https://doi.org/10.1038/srep45629

Plesa A.-C., Grott M., Tosi N., Breuer D., Spohn T., and Wieczorek M. A. 2016. How large are present-day heat flux variations across the surface of Mars? *Journal of Geophysical Research: Planets* 121:2386–2403. https://doi.org/10.1002/2016JE005126.

Putnis A., and John T. 2010. Replacement processes in the Earth's crust. *Elements* 6:159–164. https://doi.org/10.2113/gselements.6.3.159.

Righter K., Yang H., Costin G., and Downs R. T. 2008. Oxygen fugacity in the Martian mantle controlled by carbon: New constraints from the nakhlite MIL 03346. *Meteoritics & Planetary Science* 43:1709–1723. https://doi.org/10.1111/j.1945-5100.2008.tb00638.x

Schmidt M. E., Schrader C. M., and McCoy T. J. 2013. The primary fO2 of basalts examined by the spirit rover in Gusev Crater, Mars: Evidence for multiple redox states in the Martian interior. *Earth and Planetary Science Letters* 384:198–208. https://doi.org/10.1016/j.epsl.2013.10.005

Schwenzer S. P., and Kring D. A. 2013. Alteration minerals in impact-generated hydrothermal systems—Exploring host rock variability. *Icarus* 226:487–496. https://doi.org/10.1016/j.icarus.2013.06.003

Semprich J. and Simon N. S. C. 2014. Inhibited eclogitization and consequences for geophysical rock properties and delamination models: Constraints from cratonic lower crustal xenoliths. *Gondwana Research* 25:668–684. https://doi.org/10.1016/j.gr.2012.08.018

Semprich J., Schwenzer S. P., Treiman A. H., and Filiberto J. 2019. Phase equilibria modeling of low-grade metamorphic Martian rocks. *Journal of Geophysical Research: Planets* 124:681–702. https://doi.org/10.1029/2018JE005869

Smrekar S. E., Lognonné P., Spohn T., Banerdt W. B., Breuer D., Christensen U., Dehant V., Drilleau M., Folkner W., Fuji N., Garcia R. F., Giardini D., Golombek M., Grott M., Gudkova T., Johnson C., Khan A., Langlais B., Mittelholz A., Mocquet A., Myhill R., Panning M., Perrin C., Pike T., Plesa A.-C., Rivoldini A., Samuel H., Stähler S. C., van Driel M., Van Hoolst T., Verhoeven O., Weber R., and Wieczorek M. 2018. Pre-mission InSights on the interior of Mars. *Space Science Reviews* 215:1–72. https://doi.org/10.1007/s11214-018-0563-9

Sohl F. and Spohn T. 1997. The interior structure of Mars: Implications from SNC meteorites. *Journal of Geophysical Research: Planets* 102:1613–1635. https://doi.org/10.1029/96JE03419

Sohl F., Schubert G., and Spohn T. 2005. Geophysical constraints on the composition and structure of the Martian interior. *Journal of Geophysical Research: Planets* 110:E12008. 10.1029/2005JE002520

Taylor G. J. 2013. The bulk composition of Mars. *Geochemistry* 73:401–420. https://doi.org/10.1016/j.chemer.2013.09.006

Taylor S. R. and McLennan S. M. 2009. *Planetary crusts: Their composition, origin and evolution*. Cambridge: Cambridge University Press.

Ueda K., Gerya T. V., and Burg J.-P. 2012. Delamination in collisional orogens: Thermomechanical modeling. *Journal of Geophysical Research: Solid Earth* 117:B08202. https://doi.org/10.1029/2012JB009144

White R. W., Powell R., Holland T. J. B., Worley B. A. 2000. The effect of TiO_2 and Fe_2O_3 on metapelitic assemblages at greenschist and amphibolite facies conditions: Mineral equilibria calculations in the system K_2O–FeO–MgO–Al_2O_3–SiO_2–H_2O–TiO_2–Fe_2O_3. *Journal of Metamorphic Geology* 18:497–511. 10.1046/j.1525-1314.2000.00269.x

White R. W., Powell R., and Clarke G. L. 2002. The interpretation of reaction textures in Fe-rich metapelitic granulites of the Musgrave Block, central Australia: Constraints from mineral equilibria calculations in the system K_2O–FeO–MgO–Al_2O_3–SiO_2–H_2O–TiO_2–Fe_2O_3. *Journal of Metamorphic Geology* 20:41–55. https://doi.org/10.1046/j.0263-4929.2001.00349.x

White R. W., Powell R., Holland T. J. B., Johnson T. E., and Green E. C. R. 2014. New mineral activity–composition relations for thermodynamic calculations in metapelitic systems. *Journal of Metamorphic Geology* 32:261–286. https://doi.org/10.1111/jmg.12071

Wieczorek M. A. and Zuber M. T. 2004. Thickness of the Martian crust: Improved constraints from geoid-to-topography ratios. *Journal of Geophysical Research: Planets* 109:E01009. https://doi.org/10.1029/2003JE002153.

Zolotov M. Y. and Mironenko M. V. 2016. Chemical models for Martian weathering profiles: Insights into formation of layered phyllosilicate and sulfate deposits. *Icarus* 275:203–220. https://doi.org/10.1016/j.icarus.2016.04.011.

Zuber M. T., Solomon S. C., Phillips R. J., Smith D. E., Leonard Tyler G., Aharonson O., Balmino G., Bruce Banerdt W., Head J. W., Johnson C. L., Lemoine F. G., McGovern P. J., and Neumann G. A. 2000. Internal structure and early thermal evolution of mars from Mars Global Surveyor topography and gravity. *Science* 287:1788–1793. https://doi.org/10.1126/science.287.5459.1788

SUPPORTING INFORMATION

Additional supporting information may be found in the online version of this article.

Fig S1: (a-d) Calculated S-wave velocities (km/s) overlain by mineral phase diagram for compositions as in Fig. 1 (bulk compositions in Table 1).